Journal of Materials Chemistry B

ROYAL SOCIETY OF CHEMISTRY

PAPER

Published on 22 August 2026
Licence and permissions

Check for updates

Cite this: *J. Mater. Chem. B*, 2026, **14**, 10938

Fabrication of bilayer nerve conduits with sustained drug release using a multi-material, embedded 3D printing strategy

Betty Cai,[a] Sadegh Ghorbani,[ab] Lili He,[c] David Kilian,[d] Wen-Chieh Chao,[e] Jon-Paul Pepper[c] and Sarah C. Heilshorn *[a]

Received 10th August 2026,
Accepted 17th August 2026

DOI: 10.1039/d6tb01916a

rsc.li/materials-b

Nerve conduits are commonly used in peripheral nerve repair, but clinically available conduits offer limited functional recovery. While three-dimensional (3D) printing has emerged as a promising technique for nerve conduit fabrication, the fabrication of conduits with both geometrical complexity and biochemical guidance remains challenging. Here, we introduce a multi-material, embedded 3D printing approach to fabricate bilayer nerve conduits capable of sustained drug release. In this approach, bilayer conduits are formed by sequentially extruding two crosslinker-containing inks – a biomaterial ink and a sacrificial ink – into a photo-crosslinkable gel precursor support bath. As a demonstration, we fabricated conduits with a gelatin methacryloyl (GelMA)/poly(ethylene glycol) diacrylate (PEGDA)-based outer layer and fibrin-based inner layer. A decoupling of drug delivery and mechanical support is uniquely enabled by the bilayer design, where the outer layer provides mechanical strength and stability, while the inner layer enables the sustained release of nerve growth factor (NGF). The mechanical properties of bilayer conduits with varying diameters were characterized by compressive testing, and drug delivery from bilayer conduits with NGF loaded in the inner layer was quantified using *in vitro* NGF release and bioactivity assays. Finally, we demonstrated the fabrication of bilayer conduits with branched and multi-lumen geometries, which are challenging to fabricate with existing strategies. Altogether, these results highlight the promise of 3D printed nerve conduits leveraging tunable biomaterials to both physically guide and biochemically promote nerve regeneration.

1. Introduction

Peripheral nerve injury is a debilitating condition experienced by over 5 million people globally each year.[1] In severe cases, surgical repair is necessary to restore sufficient function, with ~560 000 peripheral nerve procedures being performed annually.[2] In surgical repair, nerve conduits are commonly used when the severed nerve ends do not meet. For such large-gap nerve injuries (>1 cm),[3] the conduits serve to bridge the gap between the free nerve ends, physically guiding axonal extension and preventing undesired tissue infiltration into the injury site.[4] However, clinically available nerve conduits are ineffective in fully restoring motor and sensory function: Less than 25% of patients regain normal motor function, and less than 3% regain normal sensory function.[5]

Surgical repair presents an opportunity for the localized delivery of neuromodulating factors to enhance nerve regeneration.[6] For instance, growth factors including nerve growth factor (NGF), brain-derived neurotrophic factor (BDNF), and glial cell line-derived neurotrophic factor (GDNF) have shown promise in promoting axonal regeneration.[7] However, no approved pharmacological treatments are currently available to enhance nerve repair post-injury.[8,9] To enable such treatments, nerve conduits should be developed that allow controlled drug release, have adequate mechanical strength to sustain surgical manipulation, and remain stable over the course of nerve regeneration to withstand forces exerted on the injury site.[10] Clinically available nerve conduits either employ synthetic materials, such as polyglycolic acid, or natural materials, such as porcine small intestine submucosa.[11,12] More recently, nerve allografts composed of decellularized peripheral nerve tissue have been developed.[13–15] These decellularized scaffolds preserve the native tissue microarchitecture, potentially achieving equivalent results compared to autografts in some clinical studies.[16,17] However, clinically available conduits and

[a] *Department of Materials Science and Engineering, Stanford University, Stanford, CA, 94305, USA. E-mail: heilshorn@stanford.edu*
[b] *Department of Health Technology, Technical University of Denmark, Kongens Lyngby, 2800, Denmark*
[c] *Department of Otolaryngology - Head & Neck Surgery, Stanford University, Stanford, CA, 94305, USA*
[d] *Department of Complex Tissue Regeneration, MERLN Institute of Technology-Inspired Regenerative Medicine, Maastricht University, Maastricht, 6229 ER, the Netherlands*
[e] *Department of Bioengineering, Stanford University, Stanford, CA, 94305, USA*

This journal is © The Royal Society of Chemistry 2026

allografts are not amenable to drug encapsulation, since they have a fixed material composition that is not designed for sustained drug release.

While conventional nerve conduits have single-lumen, tubular geometries, more advanced designs can more accurately mimic the native anatomy of injured peripheral nerve segments. For instance, multilayered designs can incorporate biomaterials with different functions, such as mechanical reinforcement, electrical conductance, cell encapsulation, and drug release.[18–22] Multi-lumen designs can promote cell attachment and provide more effective physical guidance to regenerating axons.[11,23] Branched conduits can be beneficial for the repair of complex nerve injuries;[24] in addition, they have been studied for preserving function of the donor nerve in nerve transfer surgeries.[25]

Recently, 3D printing has emerged as a promising approach to fabricate nerve conduits with enhanced geometrical complexity and biological functionality. Nerve conduits are commonly fabricated using either extrusion-based or digital light processing (DLP)-based 3D printing.[26] Both techniques are able to fabricate conduits with customizable, patient-specific dimensions and branching geometries. Extrusion-based 3D printing is especially suitable for fabricating multi-material conduits due to its ability to spatially pattern different biomaterial inks.[18,27] It can be applied scalably for the loading of bioactive molecules such as neurotrophic factors, since the drug–laden material is printed directly into the final construct with no inherent losses during fabrication. Furthermore, multi-material conduits can be fabricated using standard, dual-extruder bioprinters, including low-cost, open-source printer designs[28,29] and commercially available systems.[30] However, to date, nerve conduits fabricated using extrusion printing have been limited to straight, single-lumen geometries due to the physical constraints of ink deposition. In contrast, DLP-based 3D printing enables the fabrication of highly precise conduit geometries due to its high resolution. Multichannel structures can be fabricated with <100 μm wall thickness, and high-fidelity replication of the 3D model can be achieved *via* optical patterning.[31–33] However, multi-material structures require switching of the resin or resin vat, which is not possible with typical DLP setups and requires the development of custom equipment. Furthermore, loading bioactive drugs, such as neurotrophic factors, into DLP-printed conduits is typically not cost-efficient, as only a portion of the volume of the resin vat is used to form the final construct.[34]

As a subset of extrusion-based 3D printing, embedded 3D printing involves the extrusion of inks into a hydrogel or liquid support bath. This approach enables the fabrication of free-form 3D geometries without the geometrical constraints of extrusion-based approaches where inks are deposited layer by layer onto a build platform.[35–37] To fabricate hollow structures, sacrificial inks can be extruded into a crosslinkable hydrogel support bath.[38] This approach has been demonstrated for fabricating hollow structures with complex branching geometries, such as vascular-like networks.[39–42] However, this approach has not yet been applied in the fabrication of nerve conduits.

Here, we introduce a novel approach to fabricate geometrically complex, bilayer nerve conduits that release NGF using multi-material, embedded 3D printing. In this approach, two crosslinker-containing inks – a fibrinogen-based ink and a sacrificial ink – are extruded sequentially into a photocrosslinkable gel precursor support bath. A self-supporting, hollow bilayer conduit is formed *via* the diffusion of crosslinkers from the printed inks. Using this approach, we fabricated conduits with a gelatin methacryloyl (GelMA)/poly(ethylene glycol) diacrylate (PEGDA)-based outer layer, which provides mechanical strength and stability, and a fibrin-based inner layer, which provides controlled drug release. Overall, this study presents a versatile approach leveraging biomaterials design to fabricate bilayer nerve conduits with enhanced functionality.

2. Materials and methods

2.1. Material preparation

For fibrinogen-based inks, a fibrinogen stock solution was prepared by dissolving bovine fibrinogen (MP Biomedicals) at 20 wt% in phosphate-buffered saline (PBS) at 37 °C. Cellulose nanofibers (CNF) were prepared from bacterial cellulose using a previously described protocol.[43] First, commercially available, food-grade *nata de coco* (Jubes) was washed with flowing deionized water for 2–3 days. The washed *nata de coco* was blended with deionized water in a 1 : 1 ratio until homogeneous using a blender (Osterizer). The resultant CNF was concentrated *via* centrifugation at 14 000*g* for 20 minutes. Aliquots of ~500 mg were weighed before and after drying, and the CNF concentration (in w/v%) was determined as the percentage of dry mass. Aristoflex ammonium acryloyldimethyltaurate/VC copolymer (AVC, Lotioncrafter) was dissolved at 5 wt% in PBS on a shaker at 37 °C. Xanthan gum (XG, Sigma-Aldrich) was dissolved at 3 wt% in PBS while stirring with a spatula.

To prepare the fibrinogen-based ink, the fibrinogen stock solution was mixed with the appropriate viscosity modifier (CNF, AVC, or XG), a stock solution of 50 mM lithium phenyl-2,4,6-trimethylbenzoylphosphinate (LAP, Sigma-Aldrich), and PBS by stirring with a spatula until homogeneous. For imaging, fluorescent microbeads or rhodamine-labeled fibrinogen were included. Rhodamine-labeled fibrinogen was prepared using a process described previously.[44] First, bovine fibrinogen was dissolved at 10 mg mL^{-1} in 50 mM borate buffer, pH 8.5 (Thermo Scientific). NHS-rhodamine (5/6-carboxy-tetramethylrhodamine succinimidyl ester, Thermo Scientific) was dissolved at 10 mg mL^{-1} in dimethyl sulfoxide (DMSO, Fisher BioReagents) and added to the fibrinogen solution at a molar ratio of 10 : 1. The conjugation reaction was then allowed to proceed for 2 hours. The rhodamine-labeled fibrinogen was dialyzed against 4 L of 0.9% saline solution for 3 days using 10 kDa MWCO dialysis tubing, with the dialysis buffer changed twice daily. After dialysis, the fluorescently labeled fibrinogen was lyophilized and stored at −20 °C.

For the sacrificial ink, lyophilized gelatin microparticles (LifeSupport, FluidForm Inc.) were hydrated at a concentration

of 10 wt% in cold PBS. The pH of the gelatin microparticle slurry was adjusted to 7 using 1 M NaOH. To prepare a thrombin stock solution, bovine thrombin (MP Biomedicals) was dissolved at 5000 U mL^{-1} in PBS with 0.1% BSA. The thrombin stock solution was diluted and added to the gelatin microparticle ink to achieve a final concentration of 50 U mL^{-1}. For imaging, fluorescent microbeads were added to the sacrificial ink.

For the gel precursor support material, GelMA was synthesized using a protocol described previously.[41,45] Gelatin from cold water fish skin (Sigma-Aldrich) was dissolved at 20 wt% in 0.1 M carbonate–bicarbonate buffer on a shaker at 37 °C. The pH was then adjusted to 10 using 1 M NaOH. After equilibrating the solution at 70 °C, methacrylic anhydride (MAA, Sigma-Aldrich) was added at a concentration of 83 μL per gram of gelatin dropwise while stirring at 200 rpm. The reaction vessel was covered with foil and allowed to proceed for 2 hours at 70 °C. After the reaction, GelMA was precipitated by pouring the reaction mixture into an excess volume of ethanol and subsequently collected by stirring. The precipitated GelMA was then dried in a fume hood for >24 h. Finally, GelMA was dissolved in deionized water at 80–90 °C while stirring for at least 1 hour. The GelMA concentration (in w/v%) was determined as the percentage of dry mass. The support material was prepared by mixing the GelMA and CNF stock solutions with poly(ethylene glycol) diacrylate (PEGDA, average M_n 700, Sigma-Aldrich) to achieve a composition of 20 wt% GelMA + 20 wt% PEGDA + 0.3 wt% CNF. For imaging, fluorescein isothiocyanate (FITC)-labeled GelMA was added to the support material. GelMA was conjugated with FITC using a protocol described previously.[46] First, GelMA was dissolved in PBS at a concentration of 40 mg mL^{-1}. FITC (Sigma-Aldrich) was dissolved at 10 mg mL^{-1} in DMSO and added to the GelMA solution for a final concentration of 0.4 mg mL^{-1}. The reaction was allowed to proceed in the dark overnight at room temperature. The fluorescently labeled GelMA was dialyzed against deionized water for 7 days, with the dialysis volume exchanged twice daily. The dialyzed GelMA was sterile filtered through a 0.22 μm filter and lyophilized.

2.2. Rheological characterization of inks and support materials

The rheological properties of inks and support materials were measured using an ARG2 stress-controlled rheometer (TA Instruments). For support materials and fibrinogen-based inks, a 20 mm-diameter 1° cone and plate geometry was used with a 28 μm gap height. For the gelatin microparticle sacrificial ink, a 40 mm-diameter parallel plate geometry was used with a 1.0 mm gap height. Shear stress–sweep experiments were conducted over a stress range of 0.1–1000 Pa at a frequency of 1 Hz at 25 °C. Viscosity measurements were performed at shear rates of 0.1–1000 s^{-1} at 25 °C. For each material, the consistency index, flow index, and yield stress were obtained by fitting to the Herschel–Bulkley model. Self-healing measurements were performed by applying alternating strains of 0.1% and 300% at 25 °C. For the gelatin microparticle sacrificial ink, a temperature sweep experiment was performed from 25 °C to 37 °C. Three replicates were measured for each condition.

2.3. Enzymatic degradation assay

To compare degradation kinetics, 1 mL gels composed of 20 wt% GelMA, 0.3 wt% CNF, 2 mM LAP, and 0, 10, or 20 wt% PEGDA were crosslinked for 5 minutes using a 405 nm lamp (20 W, Skouphy). An accelerated degradation assay was performed by exposing the gels to 0.5 U mL^{-1} collagenase (Gibco) in PBS. Gels were incubated on an orbital shaker at 37 °C. At each timepoint, the collagenase solution was removed, and samples were weighed after blotting with a paper towel. The collagenase solution was refreshed daily until the assay endpoint.

To evaluate degradation kinetics of the inner, drug-releasing layer, 100 μL gels composed of 5% fibrin + 2% AVC + 50 U mL^{-1} thrombin were incubated for 15 min at 37 °C in a black, clear-bottom 96-well plate. 100 μL plasmin solution in PBS (Enzyme Research Laboratories Inc.; 0, 0.5, 1, 2 U mL^{-1}) was added at 37 °C, and absorbance measurements were performed at 310 nm over time using a SpectraMax M2 Microplate Reader (Molecular Devices).

2.4. 3D printing

3D printing was performed using a custom-built dual-extruder bioprinter modified from a MakerGear M2 Rev E 3D printer, as described previously.[28,47,48] For multi-material 3D printing, dual-extruder calibration in the *X* and *Y* axes was performed using a camera-assisted *XY* calibration tool (Ember Prototypes). Calibration in the *Z* axis was performed using a precision-machined reference cube.

For the 3D printing of bilayer conduits, the fibrinogen-based ink and sacrificial ink were loaded into extruders 1 and 2, respectively. Support materials were loaded in 6-well plates or Petri dishes. Print paths were designed using Rhinoceros (version 8), as described previously.[41,45] G-codes were designed to first extrude the fibrinogen-based ink using tool 1, automatically switch to tool 2 and move it to its starting position, and then extrude the sacrificial ink using tool 2. After printing is complete, diffusion of the photoinitiator was allowed to occur for a specified amount of time. The structure was then crosslinked for 5 minutes using a 405 nm lamp. The crosslinked structure was removed from the support bath using a spatula, washed thoroughly by shaking in a 50 mL conical tube containing PBS, and placed in a 50 U mL^{-1} thrombin solution at room temperature for 1 hour to ensure full fibrinogen crosslinking. Finally, the structure was incubated at 37 °C for 15 minutes to melt the gelatin microgel sacrificial ink. The ends of the structure were cut open for sacrificial ink removal, resulting in a hollow, bilayer conduit.

2.5. Lattice and filament shape fidelity analysis

To measure lattice shape fidelity, fibrinogen-based inks containing fluorescent microbeads were extruded into 3 × 3 lattices within a 20 wt% GelMA + 20 wt% PEGDA + 0.3 wt% CNF support bath. Lattices were imaged using a Leica THUNDER fluorescence microscope with a 2.5× objective. The area

 This journal is © The Royal Society of Chemistry 2026

(A) and perimeter (P) of fully enclosed windows within each lattice were obtained *via* image thresholding in Fiji (version 2.17). Printability (Pr) was calculated using the following equation:[49]

$$\mathrm{Pr} = \frac{P^2}{16A} \quad (1)$$

To assess filament shape fidelity, fibrinogen-based inks containing fluorescent microbeads were extruded into a 20 wt% GelMA + 0.1 wt% FITC–GelMA + 20 wt% PEGDA + 0.3 wt% CNF support bath. After 5–10 minutes of photoinitiator diffusion, conduits were crosslinked for 5 minutes using a 405 nm lamp. The crosslinked conduits were extracted from the support bath and washed thoroughly in PBS. Conduits were imaged using a Leica THUNDER fluorescence microscope with a 2.5× objective.

To determine the surface roughness profiles for both the top and bottom edges of a given filament, the Threshold feature in Fiji was used to automatically determine the bounding lines. For each segment of 2 mm length, the profile height (Z_x) was determined for each point (x) in the roughness profile, with N being the total number of points. The average line for each filament edge was determined by averaging the perpendicular distances at points 1 to N spaced at a predetermined interval. For all samples, the number of points (N = 768), the distance between points (d = 2.6 microns), and the total distance evaluated (L = 2 mm) were kept constant. To determine the surface roughness of each edge, the distance of each point from the average line was calculated and averaged. The average surface roughness (R_a) was then determined using the following equation:

$$R_a = \frac{|Z_1|+|Z_2|+\ldots+|Z_N|}{N} \quad (2)$$

Results from the top and bottom edges were averaged to obtain the surface roughness of each segment.

To determine the cross-sectional aspect ratio, the major and minor axis lengths of filament cross sections were quantified in Fiji. Aspect ratio was calculated as the ratio of major to minor axis lengths.

2.6. Mechanical testing of crosslinked gels and conduits

The compressive properties of gels and conduits were measured using an ARES-G2 rheometer-DMA (TA Instruments) with a 8 mm compression fixture at a rate of 0.083 mm s^{-1}. Gels composed of 20 wt% GelMA, 0.3 wt% CNF, 2 mM LAP, and 0, 10, or 20 wt% PEGDA were cast at 2 mm thickness and crosslinked for 5 min using a 405 nm lamp. After crosslinking, gels were prepared into 8 mm disks using a biopsy punch. Bilayer conduits were fabricated with a 20 wt% GelMA + 20 wt% PEGDA + 0.3 wt% CNF outer layer and 5 wt% fibrinogen + 2 wt% AVC inner layer. The compressive stiffness of conduits was calculated based on a linear regression over a displacement of 10% the conduit diameter.

Suturing of bilayer conduits was performed using a 4/0 nylon monofilament suture with a 19 mm 3/8 circle reverse cutting needle.

2.7. NGF release assay

To assess NGF release, 3D printed bilayer conduits loaded with 10 μg mL^{-1} NGF (human beta-NGF recombinant protein, PeproTech) in the inner layer were incubated in PBS with 1× Pen/Strep on an orbital shaker at 37 °C. At each timepoint, the supernatant was collected and replenished. At the assay endpoint, the remaining NGF was extracted from printed conduits using a protocol similar to those established previously.[50,51] Conduits were cut into 1 mm-thick sections and placed in extraction buffer consisting of 2 M NaCl, 1 wt% BSA, and 0.01% Triton X-100 dissolved in PBS, for 24 h at 4 °C. Samples were centrifuged at 13 000 g for 10 minutes at 4 °C, and the supernatant was taken for analysis. The released and remaining NGF amounts were measured using an human NGF beta ELISA kit (Invitrogen).

2.8. Fluorescence recovery after photobleaching (FRAP)

For FRAP measurements, gels were prepared with 20 wt% GelMA, 20 wt% PEGDA, 0.3 wt% CNF, 2 mM LAP, and 100 μg mL^{-1} of a fluorescent probe (Eosin Y disodium salt or 10, 40, or 70 kDa FITC–dextran, Sigma-Aldrich). 50 μL of material was loaded into a clear-bottom, half-area 96-well plate, then centrifuged to remove bubbles. FRAP experiments were performed at room temperature using a Leica STELLARIS 5 confocal microscope with 30 s of photobleaching (110 μm × 110 μm area, 488 nm laser, 100% intensity) and 90 s of acquisition time. Measurements were conducted before and after crosslinking for 5 min using a 405 nm lamp. Diffusion coefficients were calculated using the "frap_analysis" MATLAB program based on the Hankel transform method.[52]

2.9. PC12 and Schwann cell culture

PC12 cells (CRL-1721, ATCC) were cultured in ATCC-formulated RPMI-1640 (Gibco) with 10% heat-inactivated horse serum (HS, Gibco), 5% fetal bovine serum (FBS, Gibco), and 1× Pen/Strep (Gibco).

Rat primary Schwann cells (Kerafast) were cultured in high-glucose DMEM (Gibco) with 10% FBS (Gibco), 1× GlutaMAX (Gibco), 1× Pen/Strep (Gibco), 10 nM neuregulin (Peprotech), and 2 μM forskolin (Sigma-Aldrich). Flasks were coated with 0.01% poly-L-lysine solution (Sigma-Aldrich) for 5 minutes and 1 μg cm^{-2} laminin from human fibroblasts (Sigma-Aldrich) for 1 hour, then washed with PBS and let dry at room temperature.

2.10. NGF bioactivity assay

To assess bioactivity of NGF released from 3D printed conduits, PC12 cells were seeded at a density of 2 × 10^4 cells cm^{-2} on 24-well plates coated with poly-D-lysine (0.01%) and laminin (50 μg mL^{-1}) for 1 hour at 37 °C. After 1 day of culture, printed bilayer conduits with and without NGF were introduced in differentiation media (ATCC-formulated RPMI-1640 with 2% HS and 1× Pen/Strep). Media was refreshed 2 days after conduit introduction.

After 5 days of exposure to printed conduits, cells were fixed with 4% paraformaldehyde in PBS for 30 minutes, then washed

three times with PBS. Permeabilization was performed with 0.25% Triton X-100 in PBS for 1 hour at room temperature. Blocking was performed with 0.1% Triton X-100, 5% normal goat serum (NGS), and 0.5 wt% bovine serum albumin (BSA, Sigma-Aldrich) in PBS for 30 minutes at room temperature. A β3-tubulin primary antibody (mouse mAb, Cat. #4466, Cell Signaling Technology, 1 : 250) diluted in PBS with 2.5% NGS and 2.5 wt% BSA was applied overnight at 4 °C. Samples were then washed with PBS three times to remove unbound primary antibody. A fluorescently tagged secondary antibody (goat anti-mouse, Alexa Fluor 488, Invitrogen) was diluted at 1 : 500 in PBS with 2.5% NGS and 2.5 wt% BSA and applied for 1 hour at room temperature. After incubation with the secondary antibody, samples were washed three times with PBS. Finally, samples were incubated with 4′,6-diamidino-2-phenylindole, dihydrochloride (DAPI, Thermo Scientific, 1 μg mL^{-1}) and Alexa Fluor Plus 647 Phalloidin (Invitrogen, 0.165 μg mL^{-1}) for 1 hour at room temperature, then washed three times with PBS. Samples were imaged using a Leica STELLARIS 5 confocal microscope. Analysis of neurite extension after β3-tubulin expression was performed using Fiji with the SNT toolbox.[53]

2.11. Cell viability assay

The viability of PC12 and Schwann cells after 4 days of culture was assessed using a live/dead staining kit (Thermo Fisher Scientific). Cells were exposed to media with no NGF, media with 1 μg mL^{-1} NGF, and cast fibrin (5%) + AVC (2%) gels with 1 μg mL^{-1} NGF. PC12 cells were cultured in differentiation media (ATCC-formulated RPMI-1640 with 2% HS and 1× Pen/Strep).

2.12. Statistical analysis

All statistical analyses were performed using GraphPad Prism (version 10.1). For comparisons of filament surface roughness and cross-sectional aspect ratio, a two-way analysis of variance (ANOVA) with Tukey's multiple comparisons test was performed. Data are presented as mean ± standard deviation unless otherwise specified.

3. Results and discussion

3.1. Multi-material, embedded 3D printing strategy to fabricate bilayer conduits

To fabricate bilayer nerve conduits, we developed a multi-material, embedded 3D printing approach (Fig. 1A). In this 3D printing strategy, the conduit is crosslinked using a "diffusion-out" process that relies on interfacial diffusion of crosslinking initiators across the different materials.[41] This strategy requires the formulation of three different thixotropic hydrogels: 1) a photocrosslinkable gel precursor support bath, 2) a drug-eluting fibrinogen ink, and 3) a sacrificial ink.

The 3D printing process involves the sequential printing of a fibrinogen ink and then a sacrificial ink, followed by diffusion-induced crosslinking, and finally printed structure extraction. First, the fibrinogen-based ink is extruded into the photocrosslinkable support bath to pattern the inner layer. The fibrinogen ink includes a photoinitiator and a bioactive drug for delivery. After printing, the photoinitiator diffuses outwards from the fibrinogen filament into the photocrosslinkable support bath. Next, the conduit lumen is patterned by extruding a sacrificial ink into the printed fibrinogen filament. The sacrificial ink contains thrombin, which diffuses outwards to crosslink the surrounding fibrinogen inner layer. Upon light irradiation, a shell of support material is crosslinked around the printed fibrinogen inner layer, forming the conduit outer layer. Finally, the sacrificial ink and uncrosslinked support material are removed, generating a hollow, bilayer conduit.

The bilayer conduit is designed to serve two key functions: The outer layer should provide mechanical strength and stability, while the inner layer should enable the controlled release of encapsulated drugs (Fig. 1B).

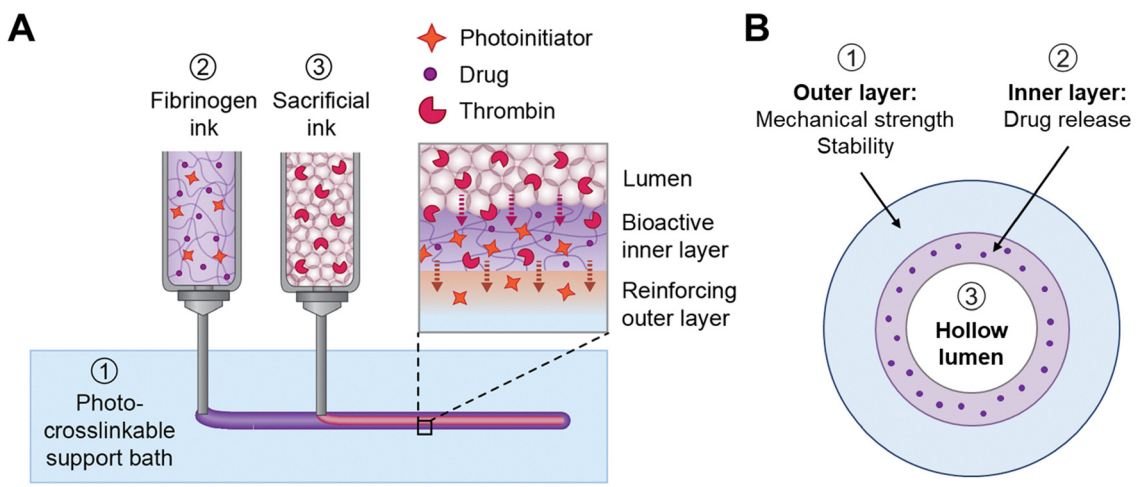


Fig. 1 Multi-material, embedded 3D printing strategy to fabricate bilayer conduits. (A) Schematic of 3D printing strategy involving the sequential extrusion of a fibrinogen-based ink and a sacrificial ink into a photocrosslinkable gel precursor support bath. (B) Schematic of resultant bilayer conduit cross section, consisting of an outer layer for mechanical reinforcement and an inner layer for drug release.

 This journal is © The Royal Society of Chemistry 2026

As a key requirement for embedded 3D printing, hydrogels with suitable rheological properties as inks and support baths must be developed. In addition, these materials must also possess suitable properties after crosslinking to form the inner and outer layers. To achieve this goal, here we design, formulate, and characterize a three-material system consisting of a photocrosslinkable GelMA/PEGDA support bath, a drug-loaded fibrinogen ink, and a gelatin microparticle sacrificial ink. These biomaterials were leveraged to fabricate drug-eluting, geometrically complex nerve guidance conduits with tunable properties for the inner and outer layers.

3.2. Design of tunable biomaterials for bilayer conduit 3D printing

In our 3D printing strategy, the conduit outer layer is formed *via* photocrosslinking of the gel precursor support bath. The outer layer material must therefore have suitable rheological properties as a support bath for embedded 3D printing. To confine printed filaments, the support bath is required to have yield-stress and self-healing behaviors. This allows the material to flow when the print nozzle passes through the bath, while re-solidifying around the ink filament after printing.[38] We achieved similar yielding behavior for all material formulations *via* the addition of cellulose nanofibers (CNF) as a viscosity modifier (Fig. 2A; Table S1). In addition, all material formulations exhibited shear-thinning and self-healing behaviors (Fig. S1). CNF is a widely used biomaterial in tissue engineering scaffolds due to its biocompatibility and controllable fibrous morphology,[54,55] and it has also been explored for use specifically in peripheral nerve repair.[56] Medical-grade sourcing can be achieved *via* biosynthesis, such as through the culture of *Komagataeibacter xylinus*.[55]

Furthermore, the outer layer material should have sufficient mechanical properties after crosslinking for future surgical use. To achieve this, we employed photocrosslinkable gel precursor formulations composed of GelMA and PEGDA. GelMA/PEGDA hydrogels have been widely applied to fabricate nerve conduits, indicating their biocompatibility and suitability for surgical implantation.[23,31,33,57] In this formulation, GelMA provides cell-binding motifs to support cell attachment, while PEGDA provides mechanical reinforcement to facilitate conduit handling as well as stability against conduit degradation. 3D printed GelMA conduits have previously been shown to support surface-guided neurite outgrowth *in vitro*,[32] and GelMA/PEGDA conduits have been shown to improve functional recovery *in vivo*.[33,58]

To tune the hydrogel mechanical properties, we tested formulations with varying concentrations of PEGDA (0, 10, and 20 wt%), while keeping the GelMA and CNF concentrations constant at 20 wt% and 0.3 wt%, respectively. After photocrosslinking, hydrogels with 10 and 20 wt% PEGDA exhibited $\sim 3\times$ and $\sim 8\times$ higher compressive moduli than 0 wt% PEGDA, respectively (Fig. 2B; Table S2).

Another important aspect of the outer layer material is its degradation profile. *In vivo*, GelMA can be degraded by physiologically present enzymes such as collagenases, and previous work has indicated the stability of GelMA hydrogels over a period of 4 weeks post-implantation in a rat model.[59] On the other hand, PEGDA primarily degrades *via* the hydrolysis of ester bonds.[60] The addition of PEGDA preserves the integrity of GelMA/PEGDA/CNF hydrogels in the presence of collagenase (Fig. 2C), thereby enhancing the stability of printed conduits. Based on these degradation profiles, a formulation of 20 wt% GelMA + 20 wt% PEGDA + 0.3 wt% CNF provided the highest stability out of the formulations tested. Given its suitable rheological properties, mechanical properties, and stability profile *in vitro*, this formulation was selected for further experiments. Importantly, the proteolytic environment after a peripheral nerve injury is complex, with multiple proteases present that change in concentration over time. Thus, to accurately evaluate the *in vivo* biodegradation profile of the selected formulation, future studies in a preclinical model of peripheral nerve injury should be performed.

For the conduit inner layer, fibrinogen was chosen as the gel precursor material. Fibrin (*i.e.* the thrombin-cleaved product of fibrinogen) is an ideal biomaterial for drug delivery due to its biocompatibility, tunable structure, and binding interactions with endogenous factors.[61,62] Fibrin hydrogels have been extensively studied for the delivery of neuromodulating factors, such as NGF, BDNF, GDNF, and neurotrophin-3.[50,51,63–66] To form the conduit inner layer, a fibrinogen-based ink is printed into the gel precursor support bath. As a result, the inner layer material should have suitable rheological properties to be extrudable while maintaining high shape fidelity after printing. To achieve this, we formulated fibrinogen-based inks using three different viscosity modifiers: CNF, ammonium acryloyldimethyltaurate/vinylpyrrolidone copolymer (AVC), and xanthan gum (XG). The shape fidelity of printed lattices was analyzed to determine suitable viscosity modifier concentrations (Fig. S2). These viscosity modifiers provide the resultant ink with yield-stress, shear-thinning, and self-healing properties (Fig. 2D–F; Table S3).

For each ink formulation, we evaluated the shape fidelity of filaments extruded into the gel precursor support bath (Fig. 2G). The fibrinogen/AVC ink had a lower surface roughness than fibrinogen/CNF and fibrinogen/XG inks when printed horizontally, while all inks formed filaments with comparable roughness when printed vertically (Fig. 2H). Similarly, the fibrinogen/AVC ink exhibited a significantly smaller cross-section aspect ratio than fibrinogen/CNF when printed horizontally, while the aspect ratios of all filaments were comparable when printed vertically (Fig. 2I).

Lastly, our 3D printing process involves the extrusion of a sacrificial ink to pattern the conduit lumen. We employed gelatin microgels, which are a commonly used sacrificial material in 3D printing.[35,67] In addition to having suitable rheological properties for printing (Fig. S3; Table S3), the gelatin microgel slurry exhibits a sol–gel transition at 34 °C (Fig. 2J), allowing it to be removed by melting.

Importantly, the previously deposited fibrinogen filament serves as a matrix for sacrificial ink extrusion. To determine the ideal inner layer material, the gelatin microgel sacrificial ink was printed into fibrinogen/CNF, fibrinogen/AVC, and fibrinogen/XG

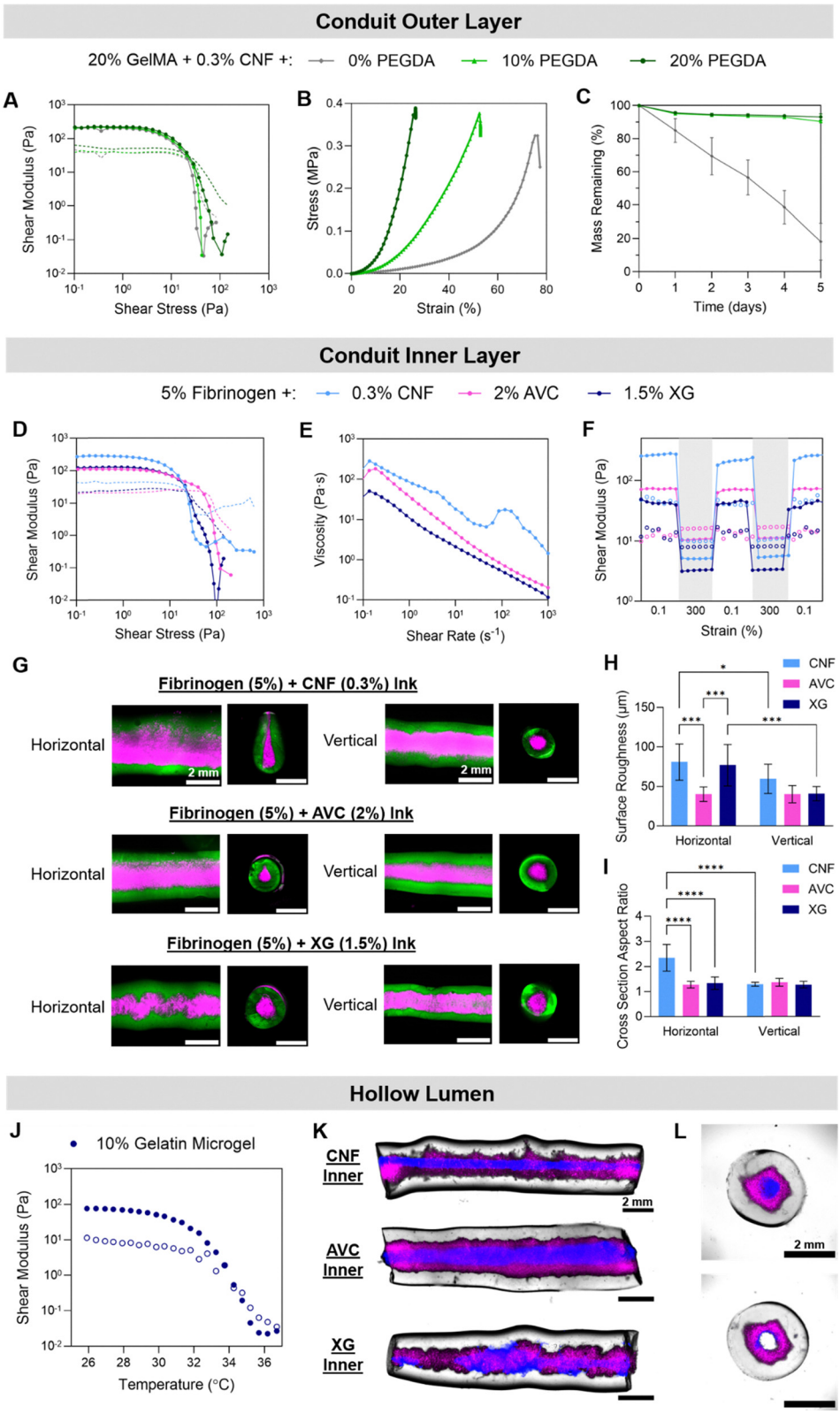


Fig. 2 Biomaterial design for bilayer conduit 3D printing. (A) Uncrosslinked support baths formulated with GelMA (20 wt%), CNF (0.3 wt%), and PEGDA (0, 10, or 20 wt%) exhibit yield-stress behavior (storage modulus G', filled circles; loss modulus G'', dashed lines). (B) The compressive moduli of crosslinked outer layer materials increase with increasing PEGDA concentration. (C) The addition of PEGDA preserves the integrity of crosslinked outer layer materials in the presence of collagenase. (D) Inks formulated with fibrinogen (5 wt%) and CNF (0.3 wt%), AVC (2 wt%), or XG (1.5 wt%) exhibit yield-stress behavior (G', filled circles; G'', dashed lines). (E) All fibrinogen-based inks are shear-thinning, facilitating extrusion through the print nozzle. (F) All fibrinogen-based inks exhibit self-healing behavior, facilitating filament shape retention after extrusion (G', filled circles; G'', hollow circles). (G) The shape

 This journal is © The Royal Society of Chemistry 2026

fidelity of fibrinogen ink filaments depends on ink formulation and printing direction (magenta: printed fibrinogen ink; green: crosslinked outer shell). (H) Fibrinogen/AVC filaments had a lower surface roughness than fibrinogen/CNF and fibrinogen/XG filaments when extruded in the horizontal direction, while all filaments had comparable surface roughness when extruded in the vertical direction (n = 8, two-way ANOVA with Tukey's multiple comparisons test, *$p < 0.05$, ***$p < 0.001$). (I) Fibrinogen/CNF filaments had a higher cross-section aspect ratio when extruded in the horizontal direction, while all filaments had comparable cross-section aspect ratios when extruded in the vertical direction (n = 5, two-way ANOVA with Tukey's multiple comparisons test, ****$p < 0.0001$). (J) The gelatin microgel sacrificial ink exhibits a sol–gel phase transition at 34 °C (G', filled circles; G'', hollow circles). (K) The shape fidelity of sacrificial ink filaments depends on the fibrinogen ink formulation (magenta: fibrin-based inner layer; blue: gelatin microgel sacrificial ink). (L) Bilayer conduits with a hollow lumen are formed after sacrificial ink removal (magenta: fibrin/AVC inner layer; blue: gelatin microgel sacrificial ink).

filaments (Fig. 2K). Both the fibrinogen/CNF and fibrinogen/AVC inks confined the sacrificial ink with high shape fidelity, while the fibrinogen/XG ink allowed for dispersal of the sacrificial ink filament.

Based on these results, the fibrinogen/AVC ink was selected for further experiments due to its lower surface roughness, higher shape fidelity, and ability to confine the printed sacrificial ink. After conduit crosslinking, the sacrificial ink was successfully removed by melting at 37 °C, while stable integration of the inner and outer layers was maintained (Fig. 2L).

Here, we demonstrate conduits of up to 3 cm in length. While longer conduits are achievable with this 3D printing method, 3 cm is considered the maximum practical gap length for conduit repair.[68] In practice, 3 cm conduits could be manufactured and cut to shorter lengths as necessary.

3.3. Control of bilayer conduit dimensions and geometry

Our multi-material, embedded 3D printing approach enables the fabrication of bilayer conduits with tunable dimensions. First, the diameter of the fibrinogen ink filament can be tuned by varying the volumetric extrusion rate (Fig. 3A). The hollow lumen diameter can similarly be controlled by varying the extrusion rate of the sacrificial ink. By varying the extrusion rates of the fibrinogen ink (E_1) and sacrificial ink (E_2), bilayer conduits with ~1–3 mm inner layer diameters and ~0.5–2 mm lumen diameters were demonstrated (Fig. 3B). Finally, the outer layer thickness can be independently modulated by varying the photoinitiator diffusion time, with thicknesses of ~0.2–0.6 mm demonstrated for diffusion times of 0.5–10 min prior to light-induced crosslinking (Fig. 3C). The dimensions of these conduits are consistent with those used for the mouse and rat sciatic nerve injury models.[20–23] Furthermore, the range of lumen diameters corresponds to that of conduits reported for human digital nerve and facial nerve repair.[69,70]

This 3D printing strategy can be readily applied to fabricate bilayer conduits with complex geometries. Bilayer conduits with freeform branching patterns can be produced by varying the print path of the ink filaments. As representative examples, a bilayer conduit with a bifurcated geometry mimicking that of a rodent sciatic nerve, and a bilayer conduit with a complex branched geometry mimicking that of a human facial nerve, were fabricated (Fig. 3D). In addition to branched conduits, multi-lumen bilayer conduits can be fabricated by patterning multiple sacrificial ink filaments into a fibrinogen ink filament (Fig. 3E). Maintenance of patency throughout multiple cross-sections along the length of a multi-lumen conduit with four channels was demonstrated (Fig. S4). By adjusting the print path and extrusion rate of the sacrificial ink, the cross-sectional geometry of these multi-lumen conduits can be readily customized. Since the conduit materials are not yet crosslinked during the sacrificial ink extrusion process, the patterning of multiple sacrificial ink filaments is not expected to affect the structural integrity of crosslinked conduits.

3.4. Mechanical characterization of 3D printed bilayer conduits

To evaluate their mechanical behavior, bilayer conduits of varying sizes (1.5–5 mm outer diameter; 0.5–2 mm hollow lumen diameter) were fabricated (Fig. 4A). Conduits with larger diameters exhibited a higher compressive stiffness in the longitudinal direction (Fig. 4B), as expected due to their larger cross-sectional area. The longitudinal stiffnesses were 0.20 ± 0.11 N mm^{-1}, 0.54 ± 0.08 N mm^{-1}, and 0.70 ± 0.15 N mm^{-1} for conduits with outer diameters of 1.5 mm, 3 mm, and 5 mm, respectively (E_1/E_2 [μL mm^{-1}] = 8/5.3, 2/1.3, and 0.8/0.4). However, larger conduits exhibited a lower compressive stiffness in the transverse direction due to greater bending of the conduit wall (Fig. 4C). For conduits with outer diameters of 1.5, 3, and 5 mm, the transverse stiffnesses were 1.28 ± 0.31 N mm^{-1}, 0.34 ± 0.07 N mm^{-1}, and 0.15 ± 0.03 N mm^{-1}, respectively. In practice, the longitudinal stiffness would determine the conduit's ability to maintain a consistent length between the nerve ends, while the transverse stiffness would determine its ability to maintain a stable, open lumen.

These mechanical properties were sufficiently robust to allow for manipulation, including actions that would be common during surgical implantation. These actions include gripping with forceps (Fig. 4D), manual bending (Fig. 4E), and suturing (Fig. 4F). These results corroborate the feasibility of fabricating printed bilayer conduits for potential surgical implantation.

3.5. Drug release from 3D printed bilayer conduits

To assess drug release characteristics, the fibrin-based inner layer of the conduits was loaded with NGF. Conduits with a fibrin (5 wt%) + AVC (2 wt%) inner layer provided sustained NGF release over a period of 12 days (Fig. 5A). In comparison, conduits with a fibrin (5 wt%) + CNF (0.3 wt%) inner layer exhibited a greater NGF release rate, with the majority of release being observed within the first 3 days (Fig. S5). We hypothesize that this difference in release may be due to electrostatic interactions between NGF, which has positively charged amino acid residues and is overall cationic (+5.8 mV at pH 7),[71] and AVC, which has negatively charged sulfonic acid moieties.[72] In addition, the conduit outer shell is expected to

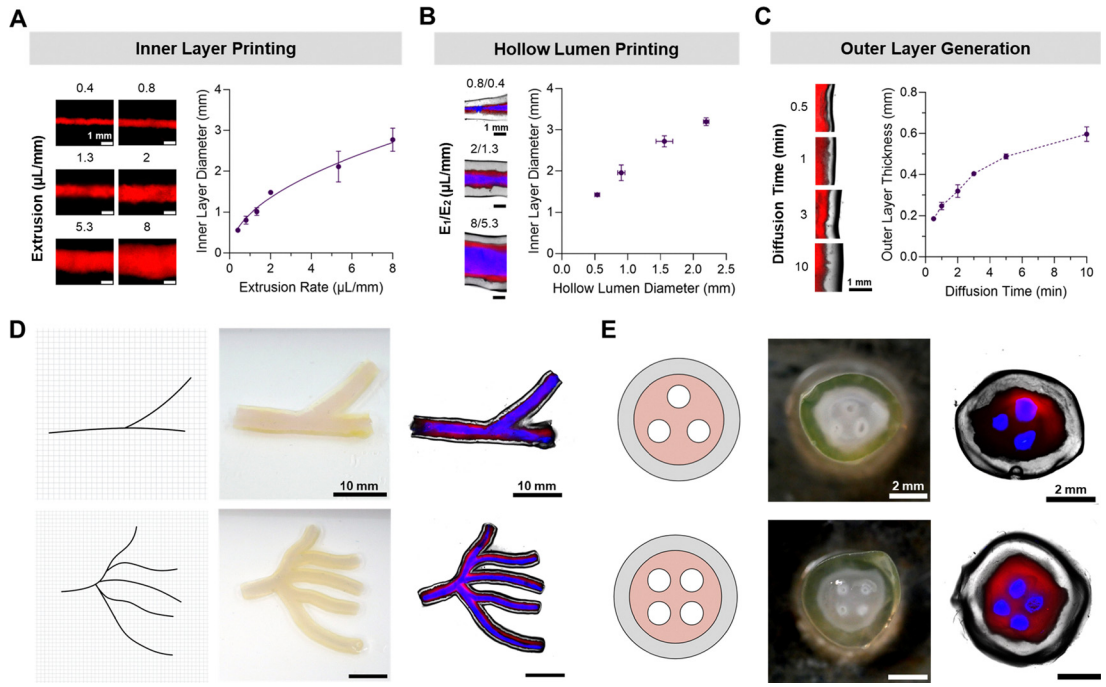


Fig. 3 Dimensional and geometrical control of 3D printed bilayer conduits. (A) The diameter of the fibrinogen ink filament (red) is controlled by the ink extrusion rate. The regression curve represents the scaling of diameter with the square root of volumetric extrusion rate (*i.e.*, volume per unit length). (B) The extrusion rates of the fibrinogen ink (E_1, red) and sacrificial ink (E_2, blue) can be varied simultaneously to produce bilayer conduits of varying sizes (from left to right: E_1/E_2 [μL mm^{-1}] = 0.8/0.4, 2/1.3, 6/3, and 8/5.3; n = 3). (C) The outer layer thickness is controlled by varying the photoinitiator diffusion time from the printed fibrinogen ink (red). (D) Branched bilayer conduits are fabricated by customizing the print path of fibrinogen and sacrificial inks. (E) Multi-lumen bilayer conduits are fabricated by extruding multiple sacrificial ink filaments within the fibrinogen ink filament. (D) and (E) Conduit design shown in left panels, photographs of printed conduits shown in middle panels, and overlaid brightfield/fluorescence micrographs shown in right panels (fibrinogen ink is red; sacrificial ink is blue).

delay diffusion of NGF out of the conduit. When crosslinked, the outerlayer GelMA/PEGDA/CNF material was found to significantly slow down the diffusion of molecules that were 10 kDa or larger in size (Fig. S6). The duration of this *in vitro*

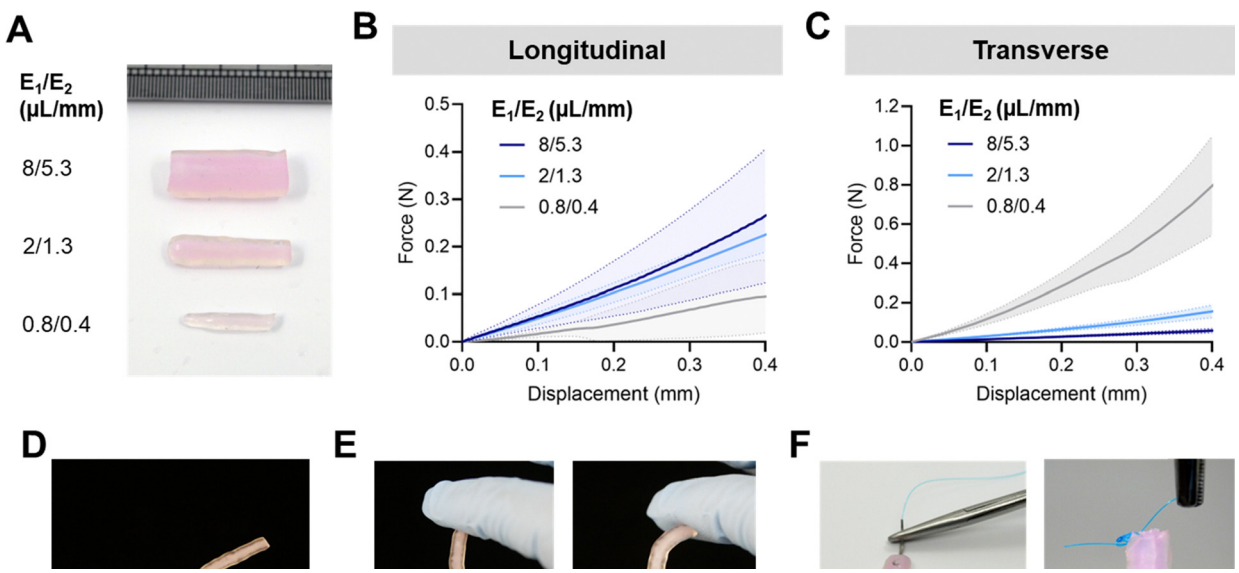


Fig. 4 Mechanical characterization of 3D printed bilayer conduits. (A) Bilayer conduits with different sizes were fabricated by varying the extrusion rates of the fibrinogen ink (E_1) and sacrificial ink (E_2). (B) Longitudinal compression of bilayer conduits of varying sizes (n = 4–5). (C) Transverse compression of bilayer conduits of varying sizes (n = 3). (D) Gripping of representative bilayer conduit (E_1/E_2 [μL mm^{-1}] = 2/1.3) with forceps. (E) Manual bending of representative bilayer conduit (E_1/E_2 [μL mm^{-1}] = 2/1.3). (F) Suturing of representative bilayer conduit (E_1/E_2 [μL mm^{-1}] = 8/5.3).

 This journal is © The Royal Society of Chemistry 2026

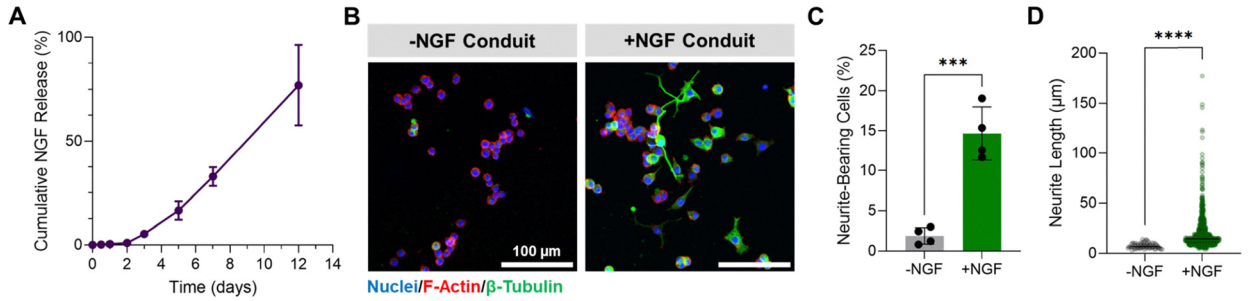


Fig. 5 Drug release from 3D printed bilayer conduits. (A) NGF release profile from the inner layer of bilayer conduits. (B) Representative immunofluorescence images of PC12 cells after 5 days of exposure to conduits with and without NGF in the inner layer. (C) Percentage of PC12 cells bearing neurites after 5 days of exposure to NGF-loaded and control conduits (N = 4 replicate conduits, unpaired t test, ***$p < 0.001$). (D) Neurite length of PC12 cells after 5 days of exposure to NGF-loaded and control conduits (n = 3672 cells for −NGF and 3747 cells for +NGF, two-tailed Mann–Whitney test, ****$p < 0.0001$, N = 4 replicate conduits). Medians are denoted by solid lines; quartiles are denoted by dotted lines.

release study over 12 days is similar in magnitude to that published in previous neurotrophin release studies (ranging from 5–14 days).[50,63]

In this experiment, the release profiles were evaluated in PBS without the presence of proteases that would be present *in vivo*. Proteases such as plasmin increase the rate of biodegradation in a dose-dependent manner (Fig. S7) and thus would impact the neurotrophin release rate. Despite this limitation, the results showcase the role of the inner layer material composition in modulating release from 3D printed conduits. Fibrin-based systems have been previously shown to support neurotrophic factor delivery over days to weeks *in vivo*.[73,74] Beyond modifying the material composition, the drug release profile may be tuned by modifying fibrinogen to have a greater binding affinity to the target drug, such as *via* functionalization with heparin-binding peptides.[75,76] Such approaches could be applied readily to the inner layer material to further modulate fibrin degradation and drug release. Future studies should further characterize neurotrophin release *in vitro* in the presence of proteases and *in vivo* using injury-specific preclinical models to finetune the desired release rate for specific clinical applications.

To confirm the bioactivity of released NGF, we evaluated its ability to induce differentiation of PC12 cells, a neuronal-like cell line. Significant neurite outgrowth was observed after 5 days of exposure to bilayer conduits with NGF loaded in the inner layer, accompanied by an increased expression of β-tubulin (Fig. 5B). Compared to conduits without NGF, a significantly greater percentage of neurite-bearing cells was observed when cells were exposed to NGF-loaded conduits (Fig. 5C). Moreover, cells exposed to NGF-loaded conduits exhibited longer neurites than those exposed to non-NGF-loaded ones (Fig. 5D). To assess the effect of NGF release on cell viability, PC-12 cells were cultured for 4 days with exposure to media with no NGF, media with NGF, and cast fibrin/AVC gels with NGF. While NGF induced neurite outgrowth in PC-12 cells, the release of NGF from cast gels did not affect cell viability (Fig. S8). These results indicate the ability of bilayer conduits to provide biological functionality *via* the release of neuroactive factors from the inner layer.

As Schwann cells are instrumental for nerve repair *in vivo*, we also assessed the effect of NGF release on Schwann cell viability (Fig. S9). High cell viability was observed for all conditions: 99.6% for media with no NGF, 99.7% for media with NGF, and 98.4% for cast fibrin/AVC gels with NGF. Future studies should further evaluate the Schwann cell phenotype *in vitro* and *in vivo* in response to the fabricated structures.

4. Conclusions

In this study, we introduced a novel 3D printing approach to fabricate bilayer nerve conduits providing both drug release and mechanical reinforcement. To enable embedded 3D printing of bilayer conduits, we designed inner and outer layer materials with suitable rheological properties as inks and support baths. After crosslinking, the GelMA/PEGDA-based outer layer of bilayer conduits provides mechanical strength and stability. Conduits with sufficient structural integrity for surgical manipulation, including gripping, bending, and suturing, were fabricated. On the other hand, the fibrin-based inner layer enables sustained release of bioactive NGF. Using a multi-material 3D printing strategy, the dimensions of the conduit lumen, inner layer, and outer layer can be independently tuned. This strategy additionally enables the fabrication of bilayer conduits with branched and multi-lumen designs, which are challenging to fabricate using existing techniques. Taken together, these results lay the foundation for future preclinical evaluation in a peripheral nerve injury model, including long-term *in vivo* studies of conduit degradation, drug release kinetics, and stability in postoperative recovery. Future work could explore the delivery of additional neuromodulating factors from printed bilayer conduits. The drug release kinetics can be tuned by varying the inner layer material composition and by modifying the binding affinity or degradability of the fibrin hydrogel. Besides neuromodulating factors, the lumen and inner layer of bilayer conduits may be seeded with therapeutic cells during the 3D printing process.[18,45] Furthermore, conductive biomaterials, such as carbon nanofibers or conducting polymer nanofibers,[57,77] can be incorporated into printed conduits to enhance neuronal growth. Altogether, this study demonstrates

the feasibility of multi-material, embedded 3D printing to fabricate nerve conduits that have the potential to both physically guide and biochemically promote nerve regeneration.

Author contributions

Conceptualization: B. C., S. G., L. H., D. K., J-P. P., and S. C. H. Investigation and methodology: B. C., S. G., L. H., D. K., and W-C. C. Funding acquisition: J-P. P. and S. C. H. Writing – original draft: B. C. Writing – review and editing: B. C., S. G., L. H., D. K., W.-C. C., J.-P. P., and S. C. H.

Conflicts of interest

S. C. H. is an inventor on a related patent (no. US20230398803A1, issued 14 December 2023) assigned to Stanford University. The remaining authors declare that they have no competing interests.

Data availability

The data that support these findings are openly available on the Stanford Digital Repositor at https://doi.org/10.25740/xq631xh8532.

Supplementary information (SI) is available. See DOI: https://doi.org/10.1039/d6tb01916a.

Acknowledgements

We thank Prof. Sungchul Shin, Dr Fotis Christakopoulos, and Neil Baugh for helpful discussions. S. C. H. acknowledges support from the National Science Foundation (DMR 2103812, DMR 2427971, and CBET 2033302), the Advanced Research Projects Agency for Health (AY1AX000002), and the National Institutes of Health (R01 EY035697, R01 MH137333, R01 HL173056). B. C. acknowledges support from the Stanford Knight-Hennessy Scholars program, Stanford Bio-X Bowes Fellowship, and the Natural Sciences and Engineering Research Council of Canada (NSERC) Postgraduate Scholarship. S.G. acknowledges support from the Novo Nordisk Foundation (NNF22OC0073507). Part of this work was performed at nano@stanford RRID:SCR_026695.

References

1 W. A. Lackington, A. J. Ryan and F. J. O'Brien, *ACS Biomater. Sci. Eng.*, 2017, **3**, 1221–1235.
2 G. Buncke, *Plast. Aesthetic Res.*, 2022, **9**, 38.
3 V. K. Singh, A. Haq, M. Tiwari and A. K. Saxena, *Injury*, 2022, **53**, 1308–1318.
4 A. Muheremu and Q. Ao, *BioMed Res. Int.*, 2015, **2015**, 237507.
5 S. Houshyar, A. Bhattacharyya and R. Shanks, *ACS Chem. Neurosci.*, 2019, **10**, 3349–3365.
6 L. He, J. E. Sato, P. Sundar, T. Azimi, P. A. Beachy, L. A. Bekale and J.-P. Pepper, *Int. J. Biol. Macromol.*, 2024, **269**, 131747.
7 S. Madduri and B. Gander, *J. Controlled Release*, 2012, **161**, 274–282.
8 A. Benga, F. Zor, A. Korkmaz, B. Marinescu and V. Gorantla, *Indian J. Plast. Surg. Off. Publ. Assoc. Plast. Surg. India*, 2017, **50**, 5–15.
9 D. Fischer, *Front. Cell Dev. Biol.*, 2025, **13**, 1558525.
10 V. Chiono and C. Tonda-Turo, *Prog. Neurobiol.*, 2015, **131**, 87–104.
11 E. Stocco, S. Barbon, A. Emmi, C. Tiengo, V. Macchi, R. De Caro and A. Porzionato, *Int. J. Mol. Sci.*, 2023, **24**, 9170.
12 C. Liu, M. Sun, L. Lin, Y. Luo, L. Peng, J. Zhang, T. Qiu, Z. Liu, J. Yin and M. Yu, *Mater. Today Bio*, 2025, **31**, 101503.
13 T. W. Hudson, S. Y. Liu and C. E. Schmidt, *Tissue Eng.*, 2004, **10**, 1346–1358.
14 M. W. McCrary, N. E. Vaughn, N. Hlavac, Y. H. Song, R. A. Wachs and C. E. Schmidt, *Tissue Eng., Part C*, 2020, **26**, 23–36.
15 R. A. Wachs, S. M. Wellman, S. L. Porvasnik, E. H. Lakes, R. C. Cornelison, Y. H. Song, K. D. Allen and C. E. Schmidt, *Cells Tissues Organs*, 2022, **212**, 512–522.
16 M. Kasper, C. Deister, F. Beck and C. E. Schmidt, *Adv. Healthcare Mater.*, 2020, **9**, 2000174.
17 B. Safa, S. Jain, M. J. Desai, J. A. Greenberg, T. R. Niacaris, J. A. Nydick, F. J. Leversedge, D. M. Megee, J. Zoldos, B. D. Rinker, D. M. McKee, B. J. MacKay, J. V. Ingari, L. J. Nesti, M. Cho, I. L. Valerio, D. S. Kao, Y. El-Sheikh, R. V. Weber, J. T. Shores, J. F. Styron, W. P. Thayer, W. H. Przylecki, H. A. Hoyen and G. M. Buncke, *Microsurgery*, 2020, **40**, 527–537.
18 J. Liu, B. Zhang, L. Li, J. Yin and J. Fu, *Bioact. Mater.*, 2021, **6**, 219–229.
19 P. Deng, F. Chen, H. Zhang, Y. Chen and J. Zhou, *Adv. Healthcare Mater.*, 2022, **11**, e2200115.
20 Y. Fang, C. Wang, Z. Liu, J. Ko, L. Chen, T. Zhang, Z. Xiong, L. Zhang and W. Sun, *Adv. Sci.*, 2023, **10**, 2205744.
21 Y. Huang, K. Ye, A. He, S. Wan, M. Wu, D. Hu, K. Xu, P. Wei and J. Yin, *Acta Biomater.*, 2024, (24), S1742–S17061.
22 X. Yang, X. Liang, B. Wang, X. Gao, W. Yang, J. Li, H. Cai, Z. Tong and Y. Chen, *Bioact. Mater.*, 2025, **51**, 46–69.
23 W.-Y. Maeng, Y. Lee, S.-H. Chen, K. S. Kim, D. Sung, W.-L. Tseng, G.-N. Kim, Y.-H. Koh, Y.-Y. Hsueh and J. Koo, *Mater. Today Bio*, 2025, **31**, 101514.
24 B. N. Johnson, K. Z. Lancaster, G. Zhen, J. He, M. K. Gupta, Y. L. Kong, E. A. Engel, K. D. Krick, A. Ju, F. Meng, L. W. Enquist, X. Jia and M. C. McAlpine, *Adv. Funct. Mater.*, 2015, **25**, 6205–6217.
25 J. Zhang, J. Tao, H. Cheng, H. Liu, W. Wu, Y. Dong, X. Liu, M. Gou, S. Yang and J. Xu, *Burns Trauma*, 2022, **10**, tkac010.
26 K. Liu, L. Yan, R. Li, Z. Song, J. Ding, B. Liu and X. Chen, *Adv. Sci.*, 2022, **9**, 2103875.
27 T. Cui, Y. Yan, R. Zhang, L. Liu, W. Xu and X. Wang, *Tissue Eng., Part C*, 2009, **15**, 1–9.
28 J. W. Tashman, D. J. Shiwarski and A. W. Feinberg, *HardwareX*, 2021, **9**, e00170.
29 J. D. Weiss, A. Mermin-Bunnell, F. S. Solberg, T. Tam, L. Rosalia, A. Sharir, D. Rütsche, S. Sinha, P. S. Choi,

 This journal is © The Royal Society of Chemistry 2026

M. Shibata, Y. Palagani, R. Nilkant, K. Paulvannan, M. Ma and M. A. Skylar-Scott, *Adv. Mater. Deerfield Beach Fla*, 2025, **37**, 2414971.
30 A. Rossi, T. Pescara, A. M. Gambelli, F. Gaggia, A. Asthana, Q. Perrier, G. Basta, M. Moretti, N. Senin, F. Rossi, G. Orlando and R. Calafiore, *Front. Bioeng. Biotechnol.*, 2024, **12**, 1393641.
31 W. Zhu, K. R. Tringale, S. A. Woller, S. You, S. Johnson, H. Shen, J. Schimelman, M. Whitney, J. Steinauer, W. Xu, T. L. Yaksh, Q. T. Nguyen and S. Chen, *Mater. Today*, 2018, **21**, 951–959.
32 W. Ye, H. Li, K. Yu, C. Xie, P. Wang, Y. Zheng, P. Zhang, J. Xiu, Y. Yang, F. Zhang, Y. He and Q. Gao, *Mater. Des.*, 2020, **192**, 108757.
33 J. Schimelman, D. B. Berry, S. Johnson, Z. R. Shi, S. Brown, Q. T. Nguyen and S. Chen, *Bioeng. Transl. Med.*, 2025, **10**, e70057.
34 J. Cheng, S. Yu, R. Wang and Q. Ge, *Int. J. Extreme Manuf.*, 2024, **6**, 042006.
35 T. J. Hinton, Q. Jallerat, R. N. Palchesko, J. H. Park, M. S. Grodzicki, H.-J. Shue, M. H. Ramadan, A. R. Hudson and A. W. Feinberg, *Sci. Adv.*, 2015, **1**, e1500758.
36 T. Bhattacharjee, S. M. Zehnder, K. G. Rowe, S. Jain, R. M. Nixon, W. G. Sawyer and T. E. Angelini, *Sci. Adv.*, 2015, **1**, e1500655.
37 C. B. Highley, C. B. Rodell and J. A. Burdick, *Adv. Mater.*, 2015, **27**, 5075–5079.
38 L. G. Brunel, S. M. Hull and S. C. Heilshorn, *Biofabrication*, 2022, **14**, 032001.
39 W. Wu, A. DeConinck and J. A. Lewis, *Adv. Mater. Deerfield Beach Fla*, 2011, **23**, H178–183.
40 M. A. Skylar-Scott, S. G. M. Uzel, L. L. Nam, J. H. Ahrens, R. L. Truby, S. Damaraju and J. A. Lewis, *Sci. Adv.*, 2019, **5**, eaaw2459.
41 S. Shin, L. G. Brunel, B. Cai, D. Kilian, J. G. Roth, A. J. Seymour and S. C. Heilshorn, *Adv. Funct. Mater.*, 2023, **33**, 2307435.
42 Y. Fang, Y. Guo, B. Wu, Z. Liu, M. Ye, Y. Xu, M. Ji, L. Chen, B. Lu, K. Nie, Z. Wang, J. Luo, T. Zhang, W. Sun and Z. Xiong, *Adv. Mater.*, 2023, **35**, 2205082.
43 J. G. Roth, L. G. Brunel, M. S. Huang, Y. Liu, B. Cai, S. Sinha, F. Yang, S. P. Paşca, S. Shin and S. C. Heilshorn, *Nat. Commun.*, 2023, **14**, 4346.
44 D. B. Kolesky, K. A. Homan, M. A. Skylar-Scott and J. A. Lewis, *Proc. Natl. Acad. Sci. U. S. A.*, 2016, **113**, 3179–3184.
45 B. Cai, D. Kilian, S. Ghorbani, J. G. Roth, A. J. Seymour, L. G. Brunel, D. R. Mejia, R. J. Rios, I. M. Szabo, S. C. Iranzo, A. Perez, R. R. Rao, S. Shin and S. C. Heilshorn, *Biofabrication*, 2025, **17**, 025012.
46 C. Onofrillo, S. Duchi, S. Francis, C. D. O'Connell, L. M. Caballero Aguilar, S. Doyle, Z. Yue, G. G. Wallace, P. F. Choong and C. Di Bella, *Biomaterials*, 2021, **264**, 120383.
47 K. Pusch, T. J. Hinton and A. W. Feinberg, *HardwareX*, 2018, **3**, 49–61.
48 S. M. Hull, C. D. Lindsay, L. G. Brunel, D. J. Shiwarski, J. W. Tashman, J. G. Roth, D. Myung, A. W. Feinberg and S. C. Heilshorn, *Adv. Funct. Mater.*, 2021, **31**, 2007983.
49 L. Ouyang, R. Yao, Y. Zhao and W. Sun, *Biofabrication*, 2016, **8**, 035020.
50 S. M. Willerth, P. J. Johnson, D. J. Maxwell, S. R. Parsons, M. E. Doukas and S. E. Sakiyama-Elbert, *J. Biomed. Mater. Res., Part A*, 2007, **80A**, 13–23.
51 M. D. Wood and S. E. Sakiyama-Elbert, *J. Biomed. Mater. Res., Part A*, 2008, **84A**, 300–312.
52 P. Jönsson, M. P. Jonsson, J. O. Tegenfeldt and F. Höök, *Biophys. J.*, 2008, **95**, 5334–5348.
53 C. Arshadi, U. Günther, M. Eddison, K. I. S. Harrington and T. A. Ferreira, *Nat. Methods*, 2021, **18**, 374–377.
54 R. J. Hickey and A. E. Pelling, *Front. Bioeng. Biotechnol.*, 2019, **7**, 45.
55 J. Moohan, S. A. Stewart, E. Espinosa, A. Rosal, A. Rodríguez, E. Larrañeta, R. F. Donnelly and J. Domínguez-Robles, *Appl. Sci.*, 2020, **10**, 65.
56 N. Carter, J. Towne and D. J. Neivandt, *Cellul. Lond. Engl.*, 2021, **28**, 2791–2803.
57 S. Das, J. Thimukonda Jegadeesan and B. Basu, *ACS Biomater. Sci. Eng.*, 2024, **10**, 1620–1645.
58 W. Ye, H. Li, K. Yu, C. Xie, P. Wang, Y. Zheng, P. Zhang, J. Xiu, Y. Yang, F. Zhang, Y. He and Q. Gao, *Mater. Des.*, 2020, **192**, 108757.
59 S. Heltmann-Meyer, D. Steiner, C. Müller, D. Schneidereit, O. Friedrich, S. Salehi, F. B. Engel, A. Arkudas and R. E. Horch, *Biomed. Mater.*, 2021, **16**, 065004.
60 M. B. Browning, S. N. Cereceres, P. T. Luong and E. M. Cosgriff-Hernandez, *J. Biomed. Mater. Res., Part A*, 2014, **102**, 4244–4251.
61 A. Breen, T. O'Brien and A. Pandit, *Tissue Eng. Part B Rev.*, 2009, **15**, 201–214.
62 P. P. Spicer and A. G. Mikos, *J. Controlled Release*, 2010, **148**, 49–55.
63 S. M. Willerth, A. Rader and S. E. Sakiyama-Elbert, *Stem Cell Res.*, 2008, **1**, 205–218.
64 A. C. Lee, V. M. Yu, J. B. Lowe, M. J. Brenner, D. A. Hunter, S. E. Mackinnon and S. E. Sakiyama-Elbert, *Exp. Neurol.*, 2003, **184**, 295–303.
65 S. H. Bhang, O. Jeon, C. Y. Choi, Y. H. K. Kwon and B.-S. Kim, *J. Biomed. Mater. Res., Part A*, 2007, **80**, 998–1002.
66 L. M. Marquardt, X. Ee, N. Iyer, D. Hunter, S. E. Mackinnon, M. D. Wood and S. E. Sakiyama-Elbert, *Tissue Eng., Part A*, 2015, **21**, 2852–2864.
67 A. Lee, A. R. Hudson, D. J. Shiwarski, J. W. Tashman, T. J. Hinton, S. Yerneni, J. M. Bliley, P. G. Campbell and A. W. Feinberg, *Science*, 2019, **365**, 482–487.
68 D. N. Deal, J. W. Griffin and M. V. Hogan, *J. Am. Acad. Orthop. Surg.*, 2012, **20**, 63–68.
69 J. Isaacs and T. Browne, *Hand N. Y. N*, 2014, **9**, 131–137.
70 Y. Nakamura, K. Takanari, K. Ebisawa, M. Kanbe, R. Nakamura and Y. Kamei, *Nagoya J. Med. Sci.*, 2020, **82**, 123–128.
71 G. Siciliano, A. D. Cillis, E. Clabassi, F. Ferrara, M. S. Chiriacò, A. Turco, C. Loiola, C. Zecca, M. T. Dell'Abate,

G. Logroscino, G. Gigli, F. Malerba and E. Primiceri, *Adv. Healthcare Mater.*, 2026, **15**, e71262.
72 L. Gandolfi and R. Galleguillos, *Rheology modifiers and consumer perception. Harry's Cosmeticology*, 9th edn, 2015, pp. 768–806.
73 S. J. Taylor, E. S. Rosenzweig, J. W. McDonald. III and S. E. Sakiyama-Elbert, *J. Controlled Release*, 2006, **113**, 226–235.
74 P. J. Johnson, A. Tatara, D. A. McCreedy, A. Shiu and S. E. Sakiyama-Elbert, *Soft Matter*, 2010, **6**, 5127–5137.
75 S. E. Sakiyama-Elbert and J. A. Hubbell, *J. Controlled Release*, 2000, **65**, 389–402.
76 D. J. Maxwell, B. C. Hicks, S. Parsons and S. E. Sakiyama-Elbert, *Acta Biomater.*, 2005, **1**, 101–113.
77 J. Xie, M. R. MacEwan, S. M. Willerth, X. Li, D. W. Moran, S. E. Sakiyama-Elbert and Y. Xia, *Adv. Funct. Mater.*, 2009, **19**, 2312–2318.

 This journal is © The Royal Society of Chemistry 2026